Strain-tunable half-metallicity in VSe_2/Sc_2CO_2 van der Waals heterostructures

Lingling Song,[1,*] Runlong Ye,[1] Chen Su,[1] Canglong Wei,[1] Dongdong Chen,[1] Xiaofeng Liu,[2] Xiaohong Zheng,[3,†] and Hua Hao[4,‡]

[1]*School of Microelectronics, Hefei University of Technology, Hefei 230601, China*
[2]*School of Physics, Hefei University of Technology, Hefei 230601, China*
[3]*College of Information Science and Technology, Nanjing Forestry University, Nanjing 210037, China*
[4]*School of Physics, Hangzhou Normal University, Hangzhou 311121, China*

(Received 6 December 2023; revised 22 February 2024; accepted 23 February 2024; published 12 March 2024)

The quest for advancing the development of next-generation nanospintronic devices has propelled extensive research into the realization and control of half-metallicity in 2D materials. Here, the multiferroic VSe_2/Sc_2CO_2 vdW heterostructures are theoretically investigated by using density functional theory to search for half-metallicity. Our theoretical exploration reveals that the VSe_2 layer showcases a unique capability to transit between semiconducting and half-metallic behavior by precisely manipulating the ferroelectric polarization states of the Sc_2CO_2 layer. We further delve into the diverse electronic properties of the VSe_2 layer within the heterostructure, employing uniaxial tensile strain engineering to investigate its behavior in both the semiconductor and half-metallic states. In the semiconductor state, this electronic property of the VSe_2 layer remains unchanged with strain. In contrast, in the half-metallic state, the VSe_2 layer undergoes a fascinating modulation, transiting from the spin-down half-metal to the metal and then to the spin-up half-metal as the strain increases from 0% to 6%. This intriguing phenomenon is elucidated by the intricate rearrangement of the inner V atomic orbitals in response to strain.

DOI: 10.1103/PhysRevB.109.094105

I. INTRODUCTION

Half-metallicity exhibits an exceptional feature, which demonstrates a metallic behavior in one spin channel and an insulating behavior in the other, leading to great potential in spintronics [1–6]. Since the initial discovery of NiMnSb Heusler alloys [4], half-metallicity have been observed in a range of other materials, like double perovskite [7], metallic oxide [8], metal-doped diluted magnetic semiconductor [9,10], etc. Especially, the widespread emergence of many two-dimensional (2D) materials has promoted the investigation and application of half-metallicity within the realm of 2D spintronics, such as graphene [11,12], black phosphorus [13], carbon nitride [14,15], MXene [16–18], transition-metal dichalcogenides (TMDs) [19,20]. In particular, the 2H-VSe_2 crystal as one of the classical TMDs has been observed to exhibit a robust ferromagnetic (FM) order that remains stable even above room temperature [21]. Extensive experiments have successfully synthesized monolayer 1T-VSe_2, and it has been found that infrared radiation can induce a phase transformation from 1T to 2H in VSe_2 samples [22]. This suggests that 2H-VSe_2 is a promising spintronics material. Nevertheless, VSe_2 is inherently a magnetic semiconductor rather than a half-metal, which causes significant difficulty for direct application as half-metallic devices.

There are many effective strategies to achieve and potentially control half-metallicity in 2D materials, like vertical integration [23], substituted doping [24], adsorption [25], and strain tuning [26,27]. Among them, by combining different 2D materials in a single stack, forming van der Waals (vdW) heterostructure [28,29], offers unparalleled platforms for discovering new physics, which are not found in a single 2D material. Especially, the integrating vdW heterostructure by single-component 2D TMDs and ferroelectric materials is a very novel pathway to produce half-metallic states. When VSe_2 comes into contact with ferroelectric materials, the transition between the half-metallic and semiconducting states in VSe_2 layer is achieved by the ferroelectric polarization reversal of the ferroelectric material [30,31]. More recently, it has been demonstrated that Janus 2H-VSeTe can be modulated from spin-up half-metal to spin-down half-metal as the biaxial strain varies from -13% to 10% [32]. Recent research has revealed that applying tensile or compressive strain within the range of -6% to 6% can transform the monolayer CrS_2 in the 1T′ phase into a spin-up or spin-down half-metal [33]. Such tunable half-metallic property about spin polarization is critical for spintronic applications.

One of the conventional approaches for altering the spin polarization orientation involves the introduction of an external magnetic field, which is not easy to operate at the nanoscale. Research shows that the spin-polarization direction of half-metal is invertible in $MnPSe_3$ as a bipolar magnetic semiconductor (BMS) when the doping type changes from electron to hole doping [34]. However, in practical applications, achieving precise control over carrier concentration in

*llsong@huft.edu.cn
†xhzheng@njfu.edu.cn
‡hhao@hznu.edu.cn

2D materials is a significant challenge. Instead of relying on external electrical or magnetic fields, strain engineering in TMDs offers an effective and convenient approach to manipulate the spin polarization of 2D magnetic materials.

In this paper, we propose a 2D multiferroic heterostructure by stacking of a VSe_2 monolayer over a ferroelectric Sc_2CO_2 monolayer, which is chosen for its inherent out-of-plane ferroelectric polarization and its favorable lattice compatibility with the VSe_2 monolayer. The electronic properties of multiferroic VSe_2/Sc_2CO_2 vdW heterostructures are systematically investigated by using density functional theory (DFT). We find that altering the ferroelectric polarization of Sc_2CO_2 enables flexible tuning of the electronic band structure of VSe_2, transiting it between semiconductor and half-metal. It is further shown that the uniaxial tensile strains along the along the x axis can induce a transition from spin-down half-metal to metal to spin-down half-metal in VSe_2 layer of VSe_2/Sc_2CO_2 P ↑ heterostructure. These results provide valuable insights into control for 2D materials and its immense potential for applications in advanced electronics and spintronics.

II. COMPUTATIONAL METHODS

The geometrical optimizations and the spin-resolved electronic structure calculations were performed with the Vienna *Ab initio* Simulation Package (VASP) [35], within the generalized gradient approximation (GGA) in the parametrization of Perdew-Burke-Ernzerhof (PBE) [36]. The interactions between valence electrons and ionic cores were described with the projector augmented wave (PAW) method [37]. A kinetic energy cutoff of 500 eV was set for the plane wave basis set. Moreover, to eliminate interactions between two neighboring vdW heterostructures, a vacuum region of around 20 Å was used along the direction perpendicular to the 2D layers. Geometrical structures were relaxed with the residual force less than 0.02 eV/Å, and the total energies were converged to 10^{-6} eV. The integration over the Brillouin zone was carried out using 13×7×1 Monkhorst-Pack k-point grid for the rectangular supercell. In addition, the semiempirical correction scheme of Grimme, DFT-D2 [38], was applied to treat the vdW weak interaction for all stacking configurations. A dipole correction was implemented to mitigate the influence of the vacuum electric field. Considering that the localized V-3d orbitals have a significant effect on the electronic structure of the heterostructure, the GGA+U method is also employed for the magnetic calculations. Based on recent research on VSe_2, the on-site Coulomb energy U and exchange parameter J were assigned values of 2 eV and 0.84 eV, respectively [39–41].

III. RESULTS AND DISCUSSION

Figures 1(a) and 1(b) depict the top and side views of the monolayer structures of 2H-VSe_2 and Sc_2CO_2, respectively, revealing their honeycomb-like structure akin to graphene. Specially, we note that a lower-energy structure made of trimmers of carbon atoms has been proposed for Sc_2CO_2 [42], which suggests that the ferroelectric phase [43] is not the most stable structure. However, since the energy barrier between these two phases reaches 0.445 eV per primitive cell, the ferroelectric phase is practically attainable and can be used for constructing ferroelectric tunnel junctions [42]. After the appropriate structural relaxation, the in-plane lattice constants of the VSe_2 monolayer are determined to be $a_1 = 3.34$ Å and $b_1 = 5.79$ Å. The corresponding lattice constants for the Sc_2CO_2 monolayer are found to be $a_2 = 3.44$ Å and $b_2 = 5.95$ Å. These values are consistent with findings that have been reported [2,30,44]. The 2D vdW VSe_2/Sc_2CO_2 multiferroic heterostructure is achieved by vertically stacking monolayer VSe_2 and Sc_2CO_2. The lattice mismatch, referred to as η, is calculated using the formula $\eta = \frac{a_2-a_1}{0.5(a_1+a_2)} \times 100\%$. In this case, the calculated lattice mismatch is found to be less than 3%, which falls within the acceptable range for the fabrication of vdW heterostructures.

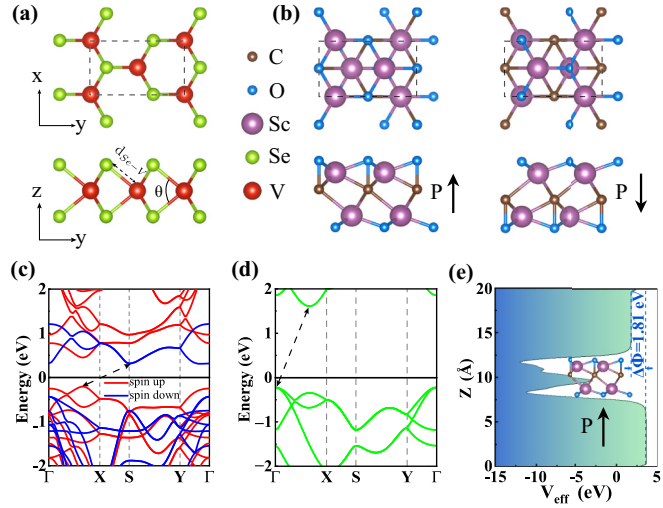

FIG. 1. The top and side views of the 2D structure of monolayer 2H-VSe_2 (a) and monolayer Sc_2CO_2 (b), respectively. The unit cell is denoted by a rectangle drawn with solid grey lines. All structures have undergone complete optimization. Band structure of monolayer 2H-VSe_2 (c) and monolayer Sc_2CO_2 (d). The Fermi level is set to zero. (e) The effective potentials (V_{eff}) along the vertical z direction to the monolayer Sc_2CO_2, in which $\Delta\Phi$ represent potential difference.

For the electronic properties, Figs. 1(c) and 1(d) present the band structures of freestanding 2H-VSe_2 monolayer and Sc_2CO_2 monolayer, respectively. Obviously, the 2H-VSe_2 monolayer is a BMS with a band gap of 0.52 eV. Specifically, the valence band maximum (VBM) originates from the spin-up channel, while the conduction band minimum (CBM) in the spin-down channel is below the CBM in the spin-up channel. This observation is in agreement with prior research [45,46]. Sc_2CO_2 exhibits nonmagnetic insulator behavior with a band gap of 1.84 eV. Additionally, monolayer Sc_2CO_2 has been theoretically proposed as an out-of-plane polarized material, and the intrinsic dipole introduces an electrostatic potential difference $\Delta\Phi = 1.81$ eV between the two surfaces of Sc_2CO_2, as shown in Fig. 1(e). Thus, there are two dynamically stable ferroelectric states in Sc_2CO_2, and the polarized state is denoted as P ↑ or P ↓, as shown in Fig. 1(b).

In the vertical VSe_2/Sc_2CO_2 multiferroic heterostructure, the ferromagnetic VSe_2 can combine with the P ↑ (P ↓) state of the ferroelectric Sc_2CO_2, resulting in the formation of a

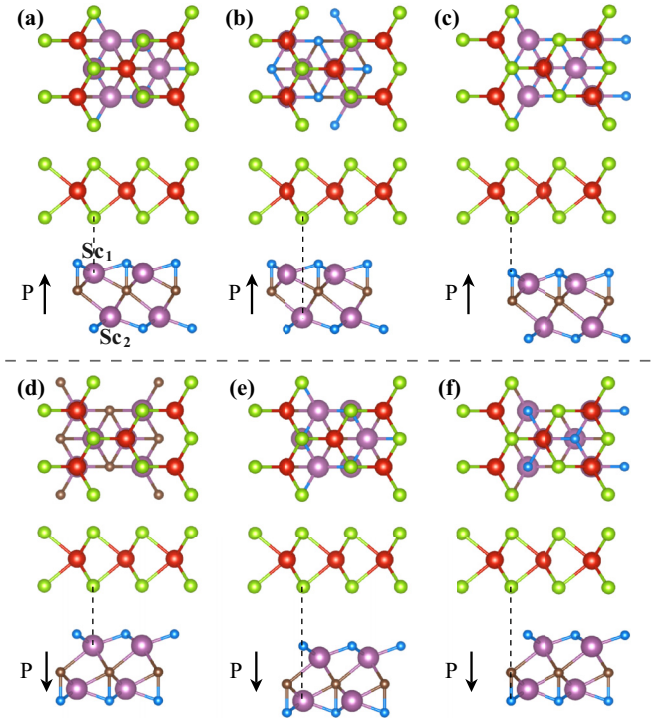

FIG. 2. [(a)–(f)] VSe_2/Sc_2CO_2 vdW heterostructures featuring diverse stacking configurations under different polarization states. For A, B, and C stacking configurations, the P ↑ and the P ↓ states are shown in (a)–(c) and (d)–(f), respectively.

heterostructure of VSe_2/Sc_2CO_2 P ↑ (VSe_2/Sc_2CO_2 P ↓). For the Sc_2CO_2 P ↑ heterostructure, three different stacking configurations, denoted as A, B, and C are considered [see Figs. 2(a)–2(c)]. The three configurations are detailed as follows: in the z direction, the Sc atoms from Sc_2CO_2 in the upper layer are defined as Sc_1, and those in the lower layer are defined as Sc_2. For the A configuration, the Se atoms in VSe_2 monolayer are directly above the Sc_1 atoms in the unit cell. For the B configuration, the Se atoms are directly above the Sc_2 atoms. For the C configuration, the Se atoms sit on the top of the vertical C-O bonds. Similarly, for the VSe_2/Sc_2CO_2 P ↓ heterostructure, three additional stacking configurations are shown in Figs. 2(d)–2(f).

In order to check the stability of the heterostructures, the binding energy E_b of the VSe_2/Sc_2CO_2 vdW heterostructure is calculated using the formula $E_b = (E_{VSe_2/Sc_2CO_2} - E_{VSe_2} - E_{Sc_2CO_2})/S$, where E_{VSe_2/Sc_2CO_2}, E_{VSe_2} and $E_{Sc_2CO_2}$ are the energy of the VSe_2/Sc_2CO_2 heterostructure, VSe_2 and Sc_2CO_2 monolayer, respectively, and S is the in-plane surface area of the considered heterostructure. The optimal interlayer distance is the one that falls within the appropriate range for achieving the minimum binding energy. Based on first-principle calculations, the binding energy E_b and the respective optimal interlayer distance d of the combined systems for all stacking configurations are listed in Table I. Negative E_b values and smaller d values indicate the energetic stability and strong physical interactions between VSe_2 and Sc_2CO_2 monolayer. The most stable structure for VSe_2/Sc_2CO_2 P ↑ is A configuration, while the most stable structure for VSe_2/Sc_2CO_2 P ↓ is C configuration, and the

TABLE I. Interface binding energies (E_b) and interlayer distance (d) of different stacking modes for VSe_2/Sc_2CO_2 heterostructures.

	VSe_2/Sc_2CO_2 ↑		VSe_2/Sc_2CO_2 ↓	
Configuration	E_b (meV/Å^2)	d (Å)	E_b (meV/Å^2)	d (Å)
A	−169.70	2.72	−152.19	3.50
B	−164.24	2.75	−152.59	2.87
C	−163.85	2.75	−154.15	2.85

top and side views of corresponding structures are shown in Figs. 4(a) and 4(b) (see below). Thus, we focus on the two most stable VSe_2/Sc_2CO_2 heterostructures as the main research objects in the following calculation.

Besides, three possible magnetic configurations including the FM, stripe-antiferromagnetic (AFM), and zigzag-AFM are considered within the $2\times\sqrt{3}\times1$ supercell as depicted in Figs. 3(a)–3(c). The relative energies ($\Delta E_m = E_{AFM} - E_{FM}$) of the FM, stripe-AFM, and zigzag-AFM structures, are shown in Table II. By GGA/PBE calculations, the energy difference between the AFM and FM ground states is always positive, suggesting that the FM ground state is more stable in the proposed VSe_2/Sc_2CO_2 heterostructures for both the polarization states.

Now, the calculated projected band structures of the VSe_2/Sc_2CO_2 P ↑ and VSe_2/Sc_2CO_2 P ↓ heterostructures are displayed in Figs. 4(c) and 4(d). After constructing vdW heterostructures, the VSe_2 layer still exhibits a significant spin polarization in its projected bands, while the spin-up and spin-down projected bands of the Sc_2CO_2 layer are nearly degenerate in energy. In the VSe_2/Sc_2CO_2 P ↑ case, the electronic states originating from the VSe_2 layer are energetically downshifted and cross the Fermi level compared to those of the free standing VSe_2 monolayer. Conversely, the electronic states originating from the Sc_2CO_2 layer are energetically upshifted and cross the Fermi level compared to those of the free standing Sc_2CO_2 monolayer. Consequently, VSe_2/Sc_2CO_2 P ↑ exhibits metallic properties, specifically with a half-metallic characteristic in the VSe_2 layer and a metallic property in the Sc_2CO_2 layer. Interestingly, the electronic structures of the heterostructure almost show the superposition of the electronic states of the VSe_2 and Sc_2CO_2 monolayer in the VSe_2/Sc_2CO_2 P ↓ case, a common band

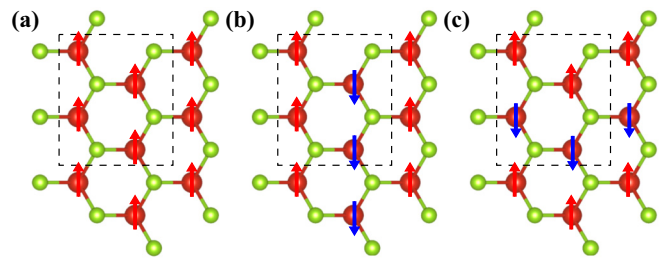

FIG. 3. Different magnetic couplings between V atoms in the VSe_2 monolayer and the proposed VSe_2/Sc_2CO_2 heterostructures. The red and blue arrows represent the spin-up and spin-down directions of V atoms, respectively. (a) The FM, and the two AFM configurations: (b) stripe-AFM, (c) zigzag-AFM.

TABLE II. The energy difference per primitive cell (ΔE_m) between FM and AFM order in the the monolayer VSe_2 and VSe_2/Sc_2CO_2 heterostructures. A zero value of ΔE_m represents the magnetic ground state.

Magnetic configuration		FM	stripe-AFM	zigzag-AFM
ΔE_m(meV)	monolayer VSe_2	0.0	106.0	108.9
	VSe_2/Sc_2CO_2 ↑	0.0	65.7	123.9
	VSe_2/Sc_2CO_2 ↓	0.0	103.2	106.9

gap is retained and the heterostructure exhibits semiconductor behavior. In short, the VSe_2 transforms from a semiconductor to a half-metal together with the switching from the P ↓ to the P ↑ state in the VSe_2/Sc_2CO_2 system. Given the metallic nature of the P ↑ vdW heterostructure, it is believed that manipulating the polarization direction of the ferroelectric layer becomes challenging due to screening effects from free electrons. Thus, this would ruin the functionality of the ferroelectric layer. However, such a situation is only limited to bulk ferroelectric metals. Cobden *et al.* proposed that a thin enough polar metal can be sufficiently penetrated by an electric field to have its polarity switched [47] and confirmed it experimentally with a ferroelectric bilayer WTe_2. A later experimental work by Chen *et al.* also confirms this conclusion [48]. These pioneering studies demonstrate the possibility of manipulating the polarization direction of 2D ferroelectric metals with an electrical field.

The observed switching behavior can be attributed to the different charge transfer across the interfaces of the VSe_2 and Sc_2CO_2 contacts, when the ferroelectric polarization is switched between the P ↑ and P ↓ states. The presence of different vacuum levels on the two surfaces of the ferroelectric Sc_2CO_2 layer results in the existence of two distinct work functions [49]. For two insulators stacked together, charge transfer occurs only when the CBM of one material falls below the VBM of the other material, resulting from the relative shift in the energy bands of the two materials [50]. Exploring the Sc_2CO_2 monolayer in different polarization states when

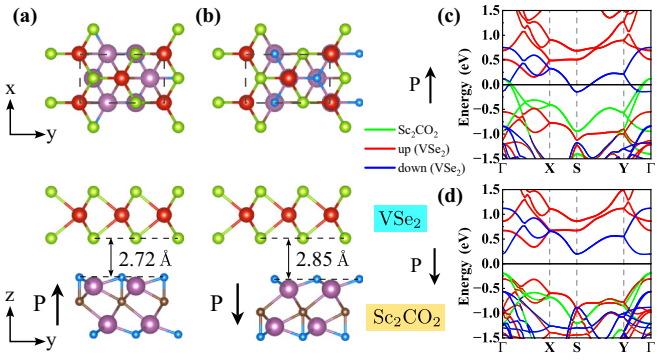

FIG. 4. (a) and (b) are the top and side views of A configuration of VSe_2/Sc_2CO_2 P ↑ vdW heterostructures and C configuration of VSe_2/Sc_2CO_2 P ↓ vdW heterostructures, respectively. Spin-resolved projected band structure of (c) A configuration of VSe_2/Sc_2CO_2 P ↑ vdW heterostructure and (d) C configuration of VSe_2/Sc_2CO_2 P ↓ vdW heterostructure. The Fermi level is set to zero.

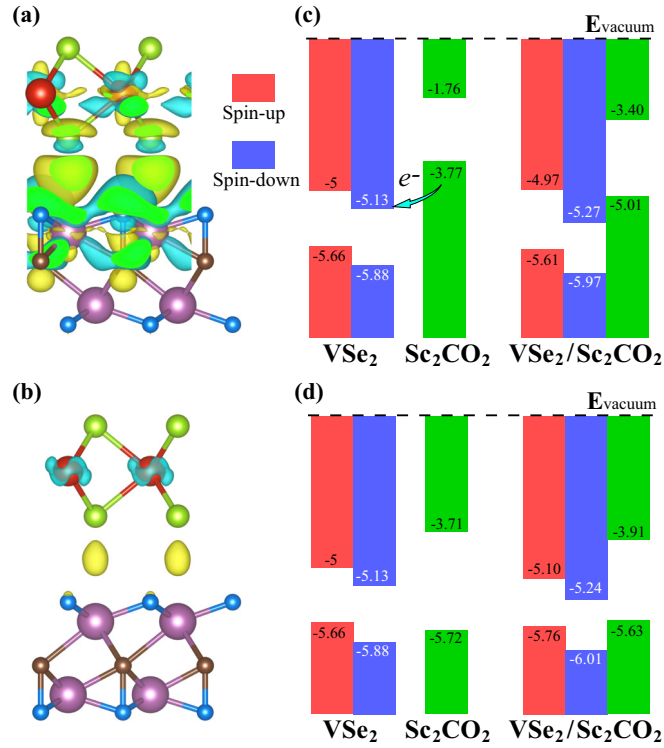

FIG. 5. The three-dimensional isosurface of the electron density difference of the multiferroic system with P ↑ (a) and P ↓ (b) states, respectively, where the yellow and blue areas represent electron accumulation and depletion, respectively. Band alignments for VSe_2/Sc_2CO_2 with ferroelectric polarization of P ↑ (c) and P ↓ (d), respectively, of isolated layers (left panel) and that after forming heterostructure (right panel). The energies are displayed in the unit of eV.

forming vdW heterostructures, as depicted in Figs. 5(a)–5(d), reveals distinctive charge transfer characteristics. When VSe_2 is combined with Sc_2CO_2 P ↑, a notable charge transfer occurs as the VBM of Sc_2CO_2 becomes energetically higher than the spin-down CBM of VSe_2. The electrons in the VBM of Sc_2CO_2 are sufficiently energetic to transit to the CBM of VSe_2. As shown in the 3D isosurface of the electron density difference of VSe_2/Sc_2CO_2 P ↑ heterostructure in Fig. 5(a), numerous electrons accumulate around the VSe_2 layer. Following our computations, the Bader charge analysis indicates a charge transfer of 0.11 e per cell during the formation of the heterostructure. As the spin-down CBM is lower than the spin-up CBM, electrons from Sc_2CO_2 predominantly migrate to the spin-down CBM of VSe_2. Due to the restricted quantity of electrons introduced into VSe_2 layer, almost no electrons occupy the spin-up CBM, resulting the spin-up CBM still above the Fermi level. As a result, the VSe_2 layer demonstrates half-metallic characteristics, as demonstrated in Fig. 5(c). In contrast, in the VSe_2/Sc_2CO_2 P ↓ case, the VBM of Sc_2CO_2 is not higher than the CBM of VSe_2, as depicted in Fig. 5(d). The built-in electric field caused by the difference in work function [50], with a vector pointing from Sc_2CO_2 layer to VSe_2 layer, induces a displacement of the energy bands in opposite directions for two materials. However, since no charge transfer occurs between two materials shown in Fig. 5(b), such

TABLE III. Binding energies (E_b) in of the heterostructures in the P ↑ and P ↓ states under tensile strain from 0% to 6%.

Strain (%)		0	1	2	3	4	5	6
E_b (meV/Å^2)	VSe_2/Sc_2CO_2 ↑	−169.7	−167.4	−165.2	−163.1	−161.3	−159.9	−158.8
	VSe_2/Sc_2CO_2 ↓	−156.7	−154.1	−151.1	−147.8	−144.3	−140.6	−136.8

effect is still insufficient to close the common band gap in the VSe_2/Sc_2CO_2 P ↓ heterostructure.

More interestingly, external factors, such as mechanical strain, can effectively and significantly modulate the electronic properties of 2D materials [27,51]. Therefore, we systematically investigate the evolution of the electronic properties of the heterostructure by in-plane uniaxial tensile strain ε along the x axis. For strain ε, it can be defined as $\varepsilon = (a - a_1)/a_1 \times 100\%$, where a represents the equilibrium lattice constant with strain application. The binding energy E_b of the VSe_2/Sc_2CO_2 vdW heterostructure in the P ↑ and P ↓ states under strains are calculated for stability analysis. The calculated values (all negative) are presented in Table III, highlighting the energetic stability of the P ↑ and the P ↓ states. Figures 6(a)–6(d) and 6(f)–6(i) show the calculated projected band structures of the P ↑ and P ↓ heterostructures within a slight strain range from 0% to 6%, respectively. In the case of VSe_2/Sc_2CO_2 P ↓, the semiconductor nature is well preserved as ε increases from 0% to 6%. In the case of VSe_2/Sc_2CO_2 P ↑, the electronic properties of the Sc_2CO_2 layer are strain insensitive, consistently demonstrating metallic properties and intrinsic spin degeneracy. In contrast, the VSe_2 layer exhibits more pronounced strain-dependent properties. When no strain is applied, as mentioned above, VSe_2 is in spin-down half-metallic states. As the strain is increased, the energy levels of CBM for spin-up and spin-down channels undergo different changes. Specifically, for the spin-up channel, the CBM moves towards lower energy and intersects with the Fermi level at approximately 2.8% strain, after which it continues to decrease. For the spin-down channel, the CBM moves towards higher energy and just fails to approach the Fermi level at 4.7% strain, beyond which it continues to increase. Consequently, between 2.8% and 4.7% strain, the VSe_2 remains as a metal. When the tensile strain is higher than 4.7%, it transforms into a spin-up half-metal. The VSe_2 layer undergoes an interesting conversion from spin-down half-metal to metal to spin-up half-metal within the entire range from 0% to 6%. Thus, the spin polarization reversal of the 2D VSe_2 layer in VSe_2/Sc_2CO_2 P ↑ can be controlled by applied strain, making it very attractive for spintronics applications.

By employing strain engineering, significant modifications can be observed in the projected band structures of VSe_2 within two heterostructures. For more accurate description, we selected the CBM of two spin channels for VSe_2 as a function of strain in the VSe_2/Sc_2CO_2 P ↑ and VSe_2/Sc_2CO_2 P ↓ heterostructures, as illustrated in Figs. 6(e) and 6(j), respectively. In terms of the energy position relative to its two spin channel CBMs and the Fermi level, the two heterostructure cases are different. For the P ↑ heterostructure,

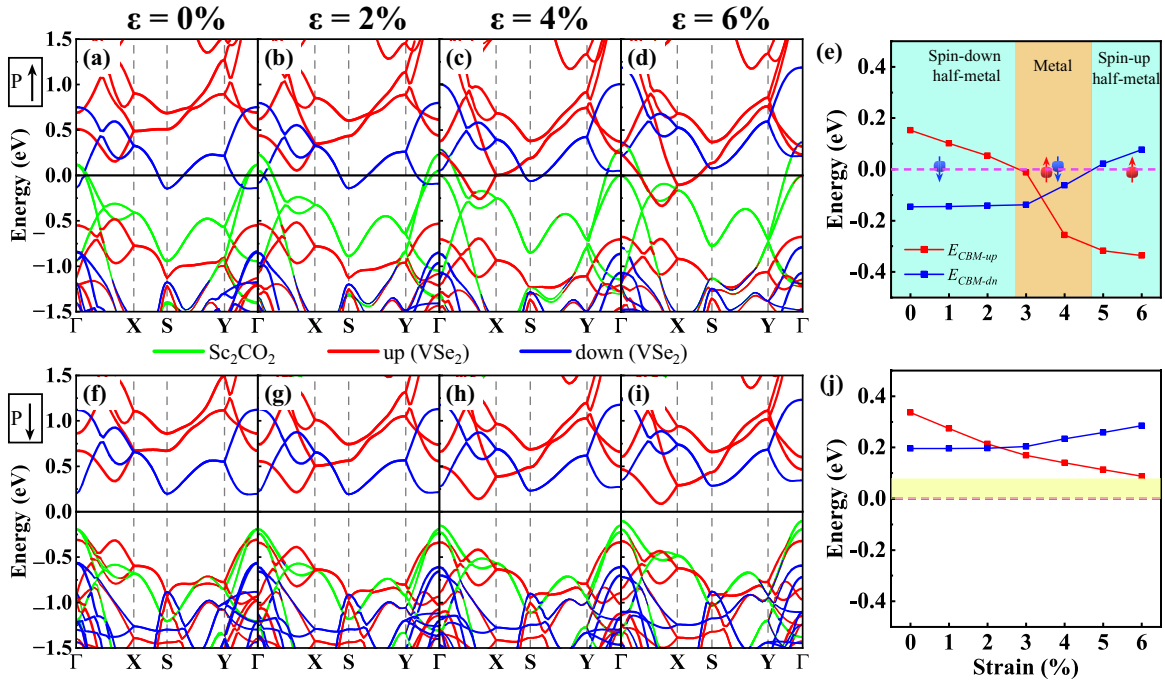

FIG. 6. Band structure of VSe_2/Sc_2CO_2 P ↑ and VSe_2/Sc_2CO_2 P ↓ at uniaxial tensile strains of (a), (f) 0%; (b), (g) 2%; (c), (h) 4%; and (d), (i) 6%. The dependence of band edges of VSe_2 layer in (e) the VSe_2/Sc_2CO_2 P ↑ and (j) VSe_2/Sc_2CO_2 P ↓ heterostructure. The Fermi level is set to zero.

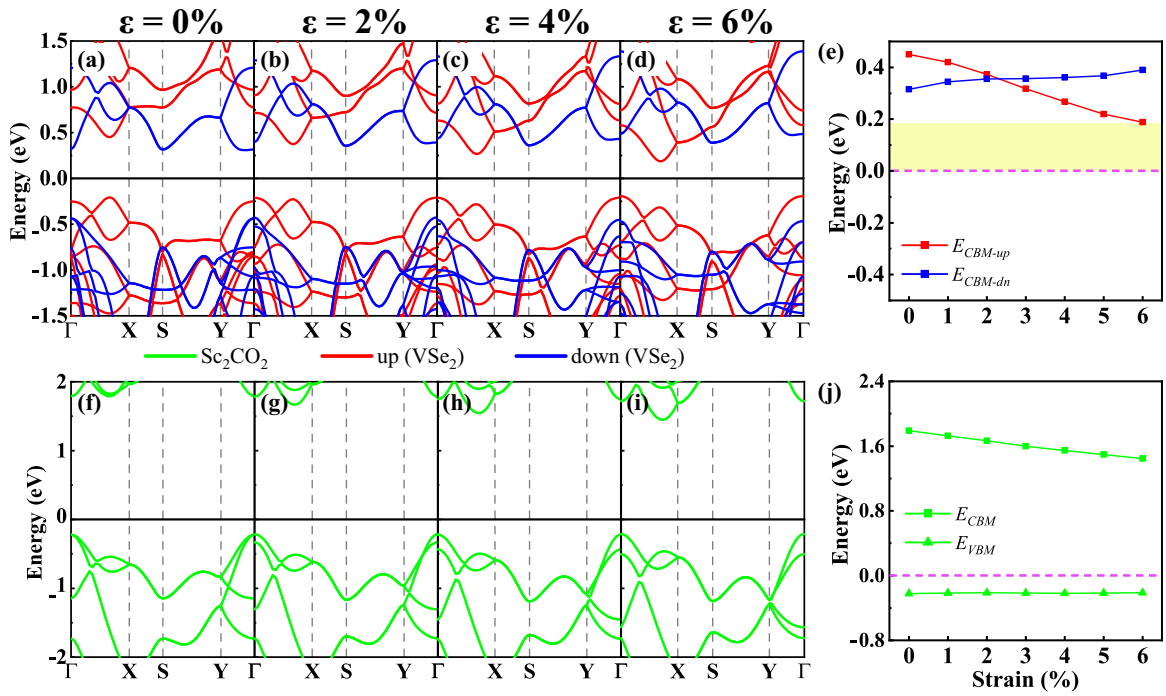

FIG. 7. Band structure of monolayer VSe_2 and Sc_2CO_2 at uniaxial tensile strains of (a), (f) 0%; (b), (g) 2%; (c), (h) 4%; and (d), (i) 6%. The dependence of band edges of VSe_2 layer in (e) the VSe_2 monolayer and (j) the Sc_2CO_2 monolayer. The Fermi level is set to zero. The red (blue) lines represent spin-up (spin-down) bands, the green lines represent Sc_2CO_2 bands, and square (triangle) lines represent the energy position of the CBM (VBM) bands.

the CBM associated with two spin channels is located near the Fermi level. This is the reason why the VSe_2 layer exhibits the most diverse electronic properties when subjected to strain engineering. For the P ↓ heterostructure, the CBM associated with the two spin channels is always above the Fermi level. Furthermore, there exists a minimum energy difference of 0.088 eV between the CBM and the Fermi level. Thus, the polarization direction of Sc_2CO_2 plays a crucial role in tuning Fermi level shifts in heterostructures. We also explore the electronic structures of the isolated monolayer VSe_2 and Sc_2CO_2 under strains in Figs. 7(a)–7(d) and 7(f)–7(i), respectively. For the Sc_2CO_2, the material always exhibits a nonmagnetic semiconductor as the strain varies. The Fermi level in this process remains almost constant relative to the VBM location [see Fig. 7(j)]. But once it combines with VSe_2 to form above heterostructures, the Fermi level experiences a substantial downward shift. For the VSe_2, the CBM variation behavior for two spin channels in monolayer VSe_2 is similar to that in VSe_2 layer of heterostructures under strains [see Fig. 7(e)]. The Fermi level also remains almost constant from $\varepsilon = 0\%$ to 6%. Once it combines with Sc_2CO_2 to form heterostructures, there is a significant increase in the Fermi level. The alterations in the band structures and band edges of monolayers of VSe_2 and Sc_2CO_2 under strain, as depicted in Fig. 7(e), demonstrate that strain has a substantial impact on two spin channels CBM in VSe_2. Consequently, this leads to diverse modifications in the properties of VSe_2/Sc_2CO_2 P ↑ heterostructure. It is well known that uniaxial strain can substantially change electronic structures due to structural variation. Geometrically speaking, the transition metal V atom is surrounded by six Se atoms in a triprismatic coordination, as depicted in Fig. 8(a). Considering that 2H-VSe_2 possesses the D_{3h} point group symmetry, so that the d orbitals of the V atom are split into three groups at different energy levels: a nondegenerate a (d_{z^2}) state, and two doubly degenerate e_1 ($d_{x^2-y^2}$, d_{xy}) and e_2 (d_{xz}, d_{yz}) states. Meanwhile, a and e_1 orbitals have the lowest energy, while e_2 orbitals are lying on higher-energy levels, as schematically illustrated in Fig. 8(b), which is consistent with our calculated band structure

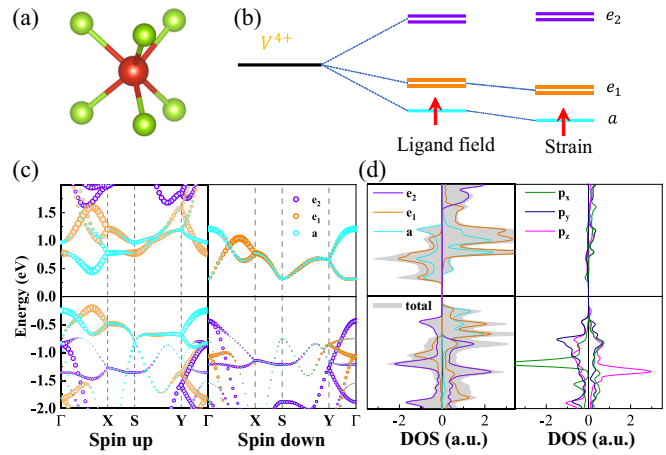

FIG. 8. (a) Structure of V^{4+} ions at the crystallographic site of D_{3h} symmetry. (b) Schematic diagram of the evolution of V^{4+} d orbitals splitting in monolayer VSe_2 under the influence of uniaxial strain. (c) Orbital resolved (left) spin-up and (right) spin-down band structures of VSe_2. (d) The partial density of states (PDOS) of (left) d-resolved orbitals (right) p-resolved orbitals of VSe_2.

TABLE IV. The bond length (d_{Se-V}) and the Se-V-Se angle (θ) under different uniaxial strains.

Strain (%)	0	1	2	3	4	5	6
d_{Se-V} (Å)	2.511	2.518	2.526	2.533	2.540	2.549	2.556
θ (°)	79.52	79.26	79.00	78.76	78.57	78.28	78.11

displayed in Fig. 8(c). To gain more physical insights into the interplay of the *d* orbitals, the spin-resolved partial density of states of VSe_2 are shown in Fig. 8(d). The electronic states of the two spin CBMs contributed mainly from *a* orbital of the V atom and feebly by the *p* orbitals of the Se atom. The crystal field deformation surrounding the V atom can be fine-tuned by exerting external strains, and further affect the Coulomb repulsion interactions between the V atom and ligands, resulting in the rearrangement of V orbitals. The *a* orbital demonstrates a predilection for participating in out-of-plane bonding with the Se atom, whereas the e_1 orbitals are conducive to in-plane bonding. Under tensile strain range from 0% to 6%, the Se-V bond length (d_{Se-V}) and the Se-V-Se angle (θ) of the VSe_2 monolayer are presented in Table IV [details are shown in Fig. 1(a)]. Structurally, as the in-plane lattice parameter is increased (under tension), the bond lengths between the V and Se atom increase and the bond angles θ decrease. This leads to a reduction in the overlap between *a* and chalcogen states, our findings align with prior researches [52–54]. With increasing strain, the Se-V bond length increases, which means that the Se atoms gradually move away from the magnetic V atoms. Thus, the interaction between the V atoms and the Se atoms becomes weaker and the *d* orbital of the V atom becomes more localized. For *d* orbitals, a stronger localization results in a more pronounced exchange-enhanced spin splitting. With the decrease in *a*-state energy (independent of spin) being taken into consideration, the spin-up conduction band drops further, while the upshift of the spin-down conduction band due to the exchange interaction is counteracted by the downshift induced by the decrease in *a*-state energy, which ultimately leads to the increasing spin splitting in the conduction band.

IV. CONCLUSIONS

In conclusion, using first-principles calculations, we determined the structural stability and electronic properties of VSe_2/Sc_2CO_2 multiferroic vdW heterostructures. Under Sc_2CO_2 P ↑, a transition from semiconductor to half-metal observed in VSe_2 layer of VSe_2/Sc_2CO_2 P ↑ heterostructure, which can be used in efficient memory devices. This transition is attributed to the presence of a built-in electric field induced by polarization and the resulting charge transfer. Besides, electronic structure calculations demonstrate that the uniaxial tensile strains along the *x* axis can induce a transition from spin-down half-metal ($0\% < \varepsilon < 2.8\%$) to metal ($2.8\% < \varepsilon < 4.7\%$) to spin-down half-metal ($\varepsilon > 4.7\%$) in VSe_2 layer of VSe_2/Sc_2CO_2 P ↑ heterostructure. Further analysis demonstrates that half-metals with adjustable spin polarization in VSe_2/Sc_2CO_2 P ↑ under strain mainly stems from the reduction of the spin-up CBM for the VSe_2 layer. In addition, we found that strains can effectively modulate the electronic structures of the spin-up CBM through the change of the Se-V distance and Se-V-Se bond angle. This characteristic enables the manipulation of strain in various regions of VSe_2/Sc_2CO_2 P ↑ heterostructure, making it easy to switch spin conduction channels for precise control of spin current. Our paper opens a promising scheme for achieving the rational control of 2D spintronics.

ACKNOWLEDGMENT

We gratefully acknowledge financial support by the National Natural Science Foundation of China under Grant No. 21503061.

[1] T. Song, X. Cai, M. W.-Y. Tu, X. Zhang, B. Huang, N. P. Wilson, K. L. Seyler, L. Zhu, T. Taniguchi, K. Watanabe, M. A. McGuire, D. H. Cobden, D. Xiao, W. Yao, and X. Xu, Giant tunneling magnetoresistance in spin-filter van der Waals heterostructures, Science **360**, 1214 (2018).

[2] P. Jiang, L. Kang, H. Hao, X. Zheng, Z. Zeng, and S. Sanvito, Ferroelectric control of electron half-metallicity in *A*-type antiferromagnets and its application to nonvolatile memory devices, Phys. Rev. B **102**, 245417 (2020).

[3] X. Li and J. Yang, First-principles design of spintronics materials, Natl. Sci. Rev. **3**, 365 (2016).

[4] R. A. de Groot, F. M. Mueller, P. G. van Engen, and K. H. J. Buschow, New class of materials: Half-metallic ferromagnets, Phys. Rev. Lett. **50**, 2024 (1983).

[5] L. Song, S. Jin, P. Jiang, H. Hao, X. Zheng, and L. Zhang, Realizing robust half-metallic transport with chemically modified graphene nanoribbons, Carbon **141**, 676 (2019).

[6] X. Tao, L. Zhang, X. Zheng, H. Hao, X. Wang, L. Song, Z. Zeng, and H. Guo, h-BN/graphene van der Waals vertical heterostructure: A fully spin-polarized photocurrent generator, Nanoscale **10**, 174 (2018).

[7] K.-I. Kobayashi, T. Kimura, H. Sawada, K. Terakura, and Y. Tokura, Room-temperature magnetoresistance in an oxide material with an ordered double-perovskite structure, Nature (London) **395**, 677 (1998).

[8] J. J. Versluijs, M. A. Bari, and J. M. D. Coey, Magnetoresistance of half-metallic oxide nanocontacts, Phys. Rev. Lett. **87**, 026601 (2001).

[9] S. Picozzi, T. Shishidou, A. J. Freeman, and B. Delley, First-principles prediction of half-metallic ferromagnetic semiconductors: V- and Cr-doped BeTe, Phys. Rev. B **67**, 165203 (2003).

[10] J. Hong and R. Q. Wu, Magnetic ordering and x-ray magnetic circular dichroism of Co doped ZnO, J. Appl. Phys. **97**, 063911 (2005).

[11] K. S. Novoselov, A. K. Geim, S. V. Morozov, D. Jiang, Y. Zhang, S. V. Dubonos, I. V. Grigorieva, and A. A. Firsov, Electric field effect in atomically thin carbon films, Science **306**, 666 (2004).

[12] K. S. Kim, Y. Zhao, H. Jang, S. Y. Lee, J. M. Kim, K. S. Kim, J.-H. Ahn, P. Kim, J.-Y. Choi, and B. H. Hong, Large-scale pattern growth of graphene films for stretchable transparent electrodes, Nature (London) **457**, 706 (2009).

[13] J. Qiao, X. Kong, Z.-X. Hu, F. Yang, and W. Ji, High-mobility transport anisotropy and linear dichroism in few-layer black phosphorus, Nat. Commun. **5**, 4475 (2014).

[14] A. Du, S. Sanvito, and S. C. Smith, First-principles prediction of metal-free magnetism and intrinsic half-metallicity in graphitic carbon nitride, Phys. Rev. Lett. **108**, 197207 (2012).

[15] H. Qiu, Z. Wang, and X. Sheng, First-principles prediction of an intrinsic half-metallic graphitic hydrogenated carbon nitride, Phys. Lett. A **377**, 347 (2013).

[16] G. Wang, Theoretical prediction of the intrinsic half-metallicity in surface-oxygen-passivated Cr_2N MXene, J. Phys. Chem. C **120**, 18850 (2016).

[17] G. Wang and Y. Liao, Theoretical prediction of robust and intrinsic half-metallicity in Ni_2N MXene with different types of surface terminations, Appl. Surf. Sci. **426**, 804 (2017).

[18] L. Jun, H. Cheng-Cai, W. Yang, Y. qian, W. Lian-Yan, and L. Deng-Feng, A promising robust intrinsic half-metallic MXene nanosheet Cr_2CuC_2 with high Curie temperature, Physica E **143**, 115276 (2022).

[19] J. He and S. Li, Two-dimensional Janus transition-metal dichalcogenides with intrinsic ferromagnetism and half-metallicity, Comput. Mater. Sci. **152**, 151 (2018).

[20] P. Cui, J. Zeng, H. Peng, J.-H. Choi, Z. Li, C. Zeng, C.-K. Shih, J. P. Perdew, and Z. Zhang, Predictive design of intrinsic half-metallicity in zigzag tungsten dichalcogenide nanoribbons, Phys. Rev. B **100**, 195304 (2019).

[21] X. Wang, D. Li, Z. Li, C. Wu, C.-M. Che, G. Chen, and X. Cui, Ferromagnetism in 2D vanadium diselenide, ACS Nano **15**, 16236 (2021).

[22] A. Ghobadi, T. G. U. Ghobadi, A. K. Okyay, and E. Ozbay, Emerging photoluminescence from defective vanadium diselenide nanosheets, Photon. Res. **6**, 244 (2018).

[23] D. Wijethunge, L. Zhang, C. Tang, S. Sanvito, and A. Du, Interfacing 2D VS_2 with Janus MoSSe: Antiferromagnetic electric polarization and charge transfer driven half-metallicity, Appl. Surf. Sci. **570**, 151129 (2021).

[24] W. Alfalasi, Y. P. Feng, and N. Tit, Designing a functionalized 2D-TMD (MoX_2, X = S, Se) hosting half-metallicity for selective gas-sensing applications: Atomic-scale study, Acta Mater. **246**, 118655 (2023).

[25] W. Ju, T. Li, X. Su, H. Li, X. Li, and D. Ma, Au cluster adsorption on perfect and defective MoS_2 monolayers: Structural and electronic properties, Phys. Chem. Chem. Phys. **19**, 20735 (2017).

[26] S. Kansara, S. K. Gupta, and Y. Sonvane, Effect of strain engineering on 2D dichalcogenides transition metal: A DFT study, Comput. Mater. Sci. **141**, 235 (2018).

[27] A. U. Rahman, Strain induces ferromagnetism in a Janus transition metal dichalcogenides: CrSTe-1H monolayer, J. Electron. Mater. **52**, 1036 (2023).

[28] K. S. Novoselov, A. Mishchenko, A. Carvalho, and A. H. C. Neto, 2D materials and van der Waals heterostructures, Science **353**, aac9439 (2016).

[29] Z. Cui, K. Bai, Y. Ding, X. Wang, E. Li, J. Zheng, and S. Wang, Electronic and optical properties of Janus MoSSe and ZnO vdWs heterostructures, Superlattices Microstruct. **140**, 106445 (2020).

[30] C. Lei, X. Xu, T. Zhang, B. Huang, Y. Dai, and Y. Ma, Nonvolatile controlling valleytronics by ferroelectricity in 2H-VSe_2/Sc_2CO_2 van der Waals heterostructure, J. Phys. Chem. C **125**, 2802 (2021).

[31] C. Hu, J. Chen, E. Du, W. Ju, Y. An, and S.-J. Gong, Ferroelectric control of band alignments and magnetic properties in the two-dimensional multiferroic VSe_2/In_2Se_3, J. Phys.: Condens. Matter **34**, 425801 (2022).

[32] Z. Guan and S. Ni, Strain-controllable high curie temperature, large valley polarization, and magnetic crystal anisotropy in a 2D ferromagnetic Janus VSeTe monolayer, ACS Appl. Mater. Interfaces **12**, 53067 (2020).

[33] K. Chen, J. Deng, Y. Yan, Q. Shi, T. Chang, X. Ding, J. Sun, S. Yang, and J. Z. Liu, Diverse electronic and magnetic properties of CrS_2 enabling strain-controlled 2D lateral heterostructure spintronic devices, npj Comput. Mater. **7**, 79 (2021).

[34] X. Li, X. Wu, and J. Yang, Half-metallicity in $MnPSe_3$ exfoliated nanosheet with carrier doping, J. Am. Chem. Soc. **136**, 11065 (2014).

[35] G. Kresse and J. Hafner, *Ab initio* molecular dynamics for liquid metals, Phys. Rev. B **47**, 558 (1993).

[36] J. P. Perdew, K. Burke, and M. Ernzerhof, Generalized gradient approximation made simple, Phys. Rev. Lett. **77**, 3865 (1996).

[37] P. E. Blöchl, Projector augmented-wave method, Phys. Rev. B **50**, 17953 (1994).

[38] S. Grimme, Semiempirical GGA-type density functional constructed with a long-range dispersion correction, J. Comput. Chem. **27**, 1787 (2006).

[39] C. Li and Y. An, Tunable magnetocrystalline anisotropy and valley polarization in an intrinsic ferromagnetic Janus 2*H*-VTeSe monolayer, Phys. Rev. B **106**, 115417 (2022).

[40] S.-J. Gong, C. Gong, Y.-Y. Sun, W.-Y. Tong, C.-G. Duan, J.-H. Chu, and X. Zhang, Electrically induced 2D half-metallic antiferromagnets and spin field effect transistors, Proc. Natl. Acad. Sci. USA **115**, 8511 (2018).

[41] B. Wu, R. Quhe, J. Yang, S. Liu, J. Shi, J. Lu, and H. Du, High-performance spin filters and spin field effect transistors based on bilayer VSe_2, Adv. Theory Simul. **4**, 2000238 (2021).

[42] S. Bae, W. Espinosa-García, Y.-G. Kang, N. Egawa, J. Lee, K. Kuwahata, M. Khazaei, K. Ohno, Y.-H. Kim, M. J. Han, H. Hosono, G. M. Dalpian, and H. Raebiger, MXene phase with C_3 structure unit: A family of 2D electrides, Adv. Funct. Mater. **31**, 2100009 (2021).

[43] A. Chandrasekaran, A. Mishra, and A. K. Singh, Ferroelectricity, antiferroelectricity, and ultrathin 2D electron/hole gas in multifunctional monolayer MXene, Nano Lett. **17**, 3290 (2017).

[44] Q. Chen, N.-Y. Wang, K.-W. Shen, and J. Sun, The effect of magnetic order on the thermal transport properties of the intrinsic two-dimensional magnet 2H-VSe_2, Phys. Chem. Chem. Phys. **25**, 9817 (2023).

[45] F. Li, K. Tu, and Z. Chen, Versatile electronic properties of VSe_2 bulk, few-layers, monolayer, nanoribbons, and nanotubes: A computational exploration, J. Phys. Chem. C **118**, 21264 (2014).

[46] M. Esters, R. G. Hennig, and D. C. Johnson, Dynamic instabilities in strongly correlated VSe_2 monolayers and bilayers, Phys. Rev. B **96**, 235147 (2017).

[47] Z. Fei, W. Zhao, T. A. Palomaki, B. Sun, M. K. Miller, Z. Zhao, J. Yan, X. Xu, and D. H. Cobden, Ferroelectric switching of a two-dimensional metal, Nature (London) **560**, 336 (2018).

[48] M. Ye, S. Hu, Y. Zhu, Y. Zhang, S. Ke, L. Xie, Y. Zhang, S. Hu, D. Zhang, Z. Luo, M. Gu, J. He, P. Zhang, W. Zhang, and L. Chen, Electric polarization switching on an atomically thin metallic oxide, Nano Lett. **21**, 144 (2021).

[49] A. Kahn, Fermi level, work function and vacuum level, Mater. Horiz. **3**, 7 (2016).

[50] A. Xie, H. Hao, C.-S. Liu, X. Zheng, L. Zhang, and Z. Zeng, Giant tunnel electroresistance in two-dimensional ferroelectric tunnel junctions constructed with a Sc_2CO_2/In_2Se_3 van der Waals ferroelectric heterostructure, Phys. Rev. B **107**, 115427 (2023).

[51] J. Zhou, Y. Gu, Y.-E. Xie, F. Qiao, J. Yuan, J. He, S. Wang, Y. Li, and Y. Zhou, Strain modulation of electronic properties in monolayer SnP_2S_6 and GeP_2S_6, Inorganics **11** 301 (2023).

[52] C.-H. Chang, X. Fan, S.-H. Lin, and J.-L. Kuo, Orbital analysis of electronic structure and phonon dispersion in MoS_2, $MoSe_2$, WS_2, and WSe_2 monolayers under strain, Phys. Rev. B **88**, 195420 (2013).

[53] Z. Sun, X. Li, Z. Zhao, Y. Zeng, Y. Wei, and J. Wang, Effects of crystal deformation on spin-valley interplay and topological phase transition: A case study on VSi_2X_4 (X = N or P) monolayers, J. Mater. Chem. C **11**, 9815 (2023).

[54] P. Lu, X. Wu, W. Guo, and X. C. Zeng, Strain-dependent electronic and magnetic properties of MoS_2 monolayer, bilayer, nanoribbons and nanotubes, Phys. Chem. Chem. Phys. **14**, 13035 (2012).